# STEREO/*Extreme Ultraviolet Imager* (EUVI) Event Catalog 2006–2012

**Markus J. Aschwanden · Jean-Pierre Wülser ·
Nariaki V. Nitta · James R. Lemen · Sam Freeland ·
William T. Thompson**

**Abstract** We generated an event catalog with an automated detection algorithm based on
the entire EUVI image database observed with the two *Solar Terrestrial Relations Observatory* (STEREO)-A and -B spacecraft over the first six years of the mission (2006–2012).
The event catalog includes the heliographic positions of some 20 000 EUV events, transformed from spacecraft coordinates to Earth-based coordinates, and information on associated GOES flare events (down to the level of GOES A5-class flares). The 304 Å wavelength turns out to be the most efficient channel for flare detection (79 % of all EUVI event
detections), while the 171 Å (4 %), 195 Å (10 %), and the 284 Å channel (7 %) retrieve
substantially fewer flare events, partially due to the suppressing effect of EUV dimming,
and partially due to the lower cadence in the later years of the mission. Due to the Sun-
circling orbits of STEREO-A and -B, a large number of flares have been detected on the
farside of the Sun, invisible from Earth, or seen as partially occulted events. The statistical
size distributions of EUV peak fluxes (with a power-law slope of $\alpha_P = 2.5 \pm 0.2$) and event
durations (with a power-law slope of $\alpha_T = 2.4 \pm 0.3$) are found to be consistent with the
fractal-diffusive self-organized criticality model. The EUVI event catalog is available online at secchi.lmsal.com/EUVI/euvi_autodetection/euvi_events.txt and may serve as a comprehensive tool to identify stereoscopically observed flare events for 3D reconstruction and
to study occulted flare events.

M.J. Aschwanden (✉) · J.-P. Wülser · N.V. Nitta · J.R. Lemen · S. Freeland
Solar and Astrophysics Laboratory, Lockheed Martin Advanced Technology Center, Dept. ADBS,
Bldg.252, 3251 Hanover St., Palo Alto, CA 94304, USA
e-mail: aschwanden@lmsal.com

W.T. Thompson
Adnet Systems Inc., NASA Goddard Space Flight Center, Greenbelt, MD 20770, USA

## 1. Introduction

Solar-flare catalogs from the current solar cycle are available in hard X-rays from the *Reuven Ramaty High Energy Solar Spectroscopic Imager* (RHESSI) during the years 2002 – 2013 (hesperia.gsfc.nasa.gov/hessidata/dbase/hessi_flare_list.txt), in soft X-rays from the *Hinode* mission during the years 2006 – 2011 (st4a.stelab.nagoya-u.ac.jp/hinode_flare/: Watanabe, Masuda, and Segawa, 2012), and in EUV from the *Solar Terrestrial Relations Observatory* (STEREO) mission for the beginning of the mission from December 2006 to July 2008 (secchi.lmsal.com/EUVI/euvi_events.txt; Aschwanden *et al.*, 2009). Flare events observed with the *Solar Dynamics Observatory* (SDO) are searchable in the web-based browser tool iSolSearch (www.lmsal.com/hek/hek_isolsearch.html), a window into the Heliophysics Events Knowledgebase (HEK): Hurlburt *et al.*, 2012). An automated flare detection algorithm that identifies flares in *Atmospheric Imaging Assembly* (AIA) data down to the GOES C-class level is operated in real-time as part of the HEK event identification scheme (Martens *et al.*, 2012). The most complete flare catalog for mid-size to large flares (on the visible hemisphere) is available from the *Geostationary Operational Environmental Satellite* (GOES), operated by the National Oceanographic and Atmospheric Administration (NOAA) and searchable on the Virtual Solar Observatory (VSO) website vso.nso.edu/cgi/catalogui/. An automated solar-flare detection algorithm with about five times higher sensitivity than the NOAA flare catalog, based on analysis of the $1 – 8$ Å GOES time profiles, has revealed over 300 000 solar-flare events over the last 37 years of 1975 – 2011 (www.lmsal.com/~aschwand/GOES/: Aschwanden and Freeland, 2012). RHESSI has a duty cycle of about 50 % due to its near-Earth orbit and thus has a corresponding fraction of flare-event completeness. SDO has a duty cycle of almost 100 % from its geosynchronous orbit. *Hinode* has a field of view that does not cover the full Sun, and thus has a flare-event coverage of 51.4 % for the *X-Ray Telescope* (XRT), 24.5 % for the *Solar Optical Telescope* (SOT), and 14.9 % for the *EUV Imaging Spectrometer* (EIS) (Watanabe, Masuda, and Segawa, 2012).

The STEREO mission consists of two twin spacecraft, A and B, which circle the Sun in opposite directions over a period of about 16 years, and thus have each a field-of-view that rotates the hemispheric view from the Earth-directed front disk to the Sun's back-side over eight years. Thus, the field-of-view is initially (2006) identical with an observer's position on Earth, becomes non-overlapping for A and B but comprises together the full-Sun during the quadrature phase (2010), and coincides for A and B at the farside after eight years (2014). Consequently, STEREO/*Extreme Ultraviolet Imager* (EUVI) has the unique capability to capture a large fraction of flares on the farside of the Sun, which are not observable from Earth, or are observed only partially above some occultation height. Moreover, a large number of flares are simultaneously observed with STEREO-A and -B, and thus can be triangulated to quantify their 3D geometric structure. In this article we document an automated flare-detection algorithm that analyzes the entire STEREO/EUVI A and B database during the first six years of the mission (2006 – 2012) and provides some statistical results. The full EUVI flare catalog is electronically accessible at secchi.lmsal.com/EUVI/euvi_autodetection/euvi_events.txt. The EUVI flare catalog information may be particularly useful to identify stereoscopically observed flare events (for 3D reconstruction studies), and to study occulted flare events (regarding their vertical structure).

## 2. The STEREO/EUVI Instruments

The *Extreme Ultra-Violet Imager* (EUVI) is a normal-incidence EUV telescope (Ritchey–Chrétien type) with a $2048 \times 2048$ pixel detector, a pixel size of $1.59''$, a field-of-view out

to 1.7 solar radii, and observes in four spectral channels (Fe IX 171 Å, Fe XII 195 Å, Fe XV 284 Å, He II 304 Å) that span the $T = 0.05 - 20$ MK temperature range. Typical exposure times (at the beginning of the mission) are $2 - 4$ seconds for 171 Å, $4 - 16$ seconds for 195 Å, and $16 - 32$ seconds for 284 Å. The stabilization of EUVI images is accomplished with a fine-pointing system that compensates for spacecraft jitter down to the subarcsecond level. Further technical details of the optics, filters, response functions, and instrument calibration are given by Wülser *et al.* (2004) and in Section 2 of Howard *et al.* (2008).

EUVI images are compressed onboard the spacecraft with the ICER algorithm, which allows one to trade higher image cadence *versus* lower image quality. Typical compression factors are on the order of $20 - 40$, without degrading the image quality more than the photon noise in areas that record more than a few photons per pixel. The EUVI is typically operated in one of two modes: the synoptic mode, or the campaign mode. The basic EUVI synoptic mode has a fast cadence of 2.5 minutes for 171 Å, a slower cadence of ten minutes for 195 and 304 Å, and 20 minutes for 284 Å, at the beginning of the mission. A higher cadence of 75 seconds for 171 Å and five minutes in the other wavelengths was used during special campaigns (for two weeks in May 2007). In the later years of the mission, the 171 Å and 284 Å channel were operated with low cadences on the order of 120 minutes, which is insufficient to detect small flares.

Also, a ring buffer records EUVI images with a higher cadence during up to four hours per day, which are downloaded when extra telemetry is available. The telemetry drops stepwise with increasing distance of the STEREO spacecraft from Earth, reaching a minimum at the conjunction point behind the Sun (expected to be in 2014). The decreasing telemetry also imposes a decreasing cadence of EUV images, which affects the completeness of flare detection with progress of the mission.

## 3. The STEREO/EUVI Event Catalog

### 3.1. Automated Event Detection Method

There is a fast and a slow method to automatically detect flare events in the EUVI database. The quick method reads only the FITS headers of each image file, which contain the information of the flux maximum (FITS descriptor DATAMAX) in each image, from which full-Sun flux–time profiles can be created that are sufficient to identify the largest flares with some certainty (at GOES M- and X-class level), but without spatial information. However, for smaller flares (of GOES C-class and B-class), the variability of the EUV emission from the quiet Sun, bright points, explosive events, filaments, and prominences is of comparable magnitude as small flares, and thus small-to-intermediate flare events cannot be identified unambiguously from such full-Sun EUV time profiles. Therefore, in order to create a deep survey of EUV flare events, we have to choose the slow method, which means reading and calibrating all observed EUVI images (which are stored as compressed files and need to be uncompressed for calibration with the IDL procedure SECCHI_PREP). The calibration with SECCHI_PREP converts the observed datanumber per pixel to a normalized exposure time of one second (in units of $DN\,s^{-1}$), subtracts a dark-current bias, normalizes to open-filter position, and applies a calibration factor.

The first step of our automated event-detection algorithm is the generation of $64 \times 64$ daily time profiles extracted from the $2048 \times 2048$ pixel images, which represent the average flux $[f_{ij}^{\lambda,sc}(t)]$ in macropixels with a size of $2048/64 = 32$ pixels ($\approx 50'' \approx 36$ Mm), for each image position $i = 1, \ldots, 64$ and $j = 1, \ldots, 64$, wavelength $\lambda = 171, 195, 284, 304$ Å,
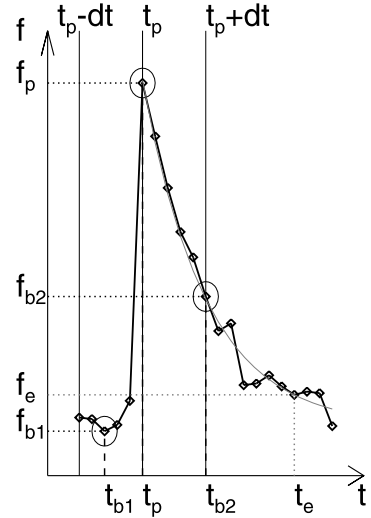
and spacecraft $[sc] = A, B$. From the $N = 64 \times 64 = 4096$ time profiles per wavelength and spacecraft we retain only the $N_{loc} = 10$ daily time profiles with the highest fluxes, which are generally sufficient to cover all active regions with flaring activity, while the other time profiles mostly belong to the quiet Sun and coronal holes and are ignored in the further analysis. The Sun has a radius of about 600 pixels in an EUVI image, and thus the ten macropixels with the largest flux variability cover about a fraction of $q_{Sun} = (10 \times 32^2)/(\pi 600^2) \approx 1\%$ of the full-Sun disk, but reduce the number of time profiles by a factor of $4096/10 \approx 400$. The accuracy of the heliographic position inferred from these macropixels (with a size of 32 pixels) is thus $\pm 16$ pixels ($\approx 25'' \approx 18$ Mm $\approx 0.025$ R$_\odot$), or $\pm 1.5°$ heliographic degrees near disk center.

The second step of the flare-detection algorithm consists of identifying impulsive increases of EUV emission in the previously sampled time profiles $[f(t) = f_{ij}^{\lambda,sc}(t)]$. For each macropixel we detect the maximum flux during a daily time interval and select for this day those ten time profiles that exhibit the largest fluxes (on the solar disk) among all $64 \times 64 = 4096$ time profiles extracted from each macropixel. Then we add up these ten time profiles into a synthesized profile. This combined EUV time profile includes only the brightest active-region areas and has a much higher contrast between impulsive flux enhancements and the slowly varying background flux than the full-Sun EUV time profiles.

For each temporal flux maximum $[f_p = f(t = t_p)]$ at time $t_p$ we determine a preflare-background flux level $[f_{b1}]$ at time $t_{b1}$ in a time interval $[(t_p - dt) < t_{b1} < t_p]$, and a postflare flux minimum $[f_{b2}]$ at time $t_{b2}$ with $[t_p < t_{b2} < (t_p + dt)]$ and $[dt] = 0.5$ hours (Figure 1). Performing a linear background interpolation between the flux minima $[f_{b1}]$ and $[f_{b2}]$,

$$f_b(t_p) = f_{b1} + (f_{b2} - f_{b1})\frac{(t_p - t_{b1})}{(t_{b2} - t_{b1})}, \tag{1}$$

we obtain a background level $[f_b(t = t_p)]$ at the peak time $t_p$. A flare event (at peak time $t_p = f(t = t_p)$) is defined by a flux enhancement that exceeds a background threshold level of $q_{thresh} = 3\%$,

$$q = \left(\frac{f_p(t = t_p)}{f_b(t = t_p)} - 1\right) \geq q_{thresh}. \tag{2}$$

The threshold level of $q_{\mathrm{thresh}} = 3\,\%$ has been chosen to optimize the detection of events down to about the GOES A5-class flare level. This sensitivity level is far above the photon noise level of EUVI data. For instance, the typical quiet-Sun level for the EUVI wavelength channels produces about 100 photons per pixel and second in the 171 Å wavelength (Howard *et al.*, 2008), which corresponds to $N \approx 10^6$ photons per macropixel and second, and has a Poisson noise of $\sqrt{N}/N \approx 10^{-3}$ or 0.1 %. The least-sensitive channel is 284 Å with a quiet-Sun level of four photons per pixel and second, which corresponds to $N \approx 4000$ photons per macropixel and second, and a Poisson noise of $\sqrt{N}/N \approx 0.015$ or 1.5 %. Furthermore, since we analyze only the brightest temporal profiles from active regions and exclude those from the quiet Sun, the significance level of the detected events is even higher. The significance level of each detected event can also be inspected *a posteriori*, since we provide the background fluxes $[f_{\mathrm{b}}]$ and flux enhancements $[f_{\mathrm{p}} - f_{\mathrm{b}}]$ in the EUVI event catalog.

Once an event with a significant temporal flux maximum is located at time $t_{\mathrm{p}}$ in the synthesized temporal profile of the macropixel $[i, j]$, the location $[i_{\mathrm{p}}, j_{\mathrm{p}}]$ of the event is identified (from the $N_{\mathrm{loc}} = 10$ possible positions) by that macropixel that has the highest flux enhancement $[q = f_{ij}^{\lambda,\mathrm{sc}}(t_{\mathrm{p}})/b_{ij}^{\lambda,\mathrm{sc}}(t_{\mathrm{p}})]$ relative to the background flux $[b_{ij}^{\lambda,\mathrm{sc}}]$, for which the heliographic longitude and latitude $[l_{\mathrm{p}}, b_{\mathrm{p}}]$ can be calculated.

For the temporal resolution of the extracted temporal profiles we set a lower limit of $\Delta t \geq 0.1$ hour (or six minutes), which is sufficient for flare detection, but reduces the amount of reading unnecessary images up to a factor of five during days with the highest cadence (75 seconds) in campaign mode. There are a few gaps in the EUVI/A and B data (mostly at the beginning of the mission). EUVI/A started taking data on 4 December 2006, while EUVI started at 14 December 2006, and the initial testing phase lasted up to March 2007, before regular temporal cadences were used for observations. Such data gaps or periods when the spacecraft was rotated produce discontinuities in the EUV temporal profiles, which were flagged by visual inspection and eliminated in the flare detection algorithm. A list of all data gaps (including data drop-outs, bad data, or instrumental anomalies) that were excluded in the automated flare detection algorithm is available (secchi.lmsal.com/EUVI/euvi_autodetection/euvi_gaps.txt).

3.2. Heliographic Event Location

All information that is needed to convert heliographic coordinates from the STEREO/A or B spacecraft coordinate system to an Earth-based coordinate system can be extracted from the FITS descriptors of the EUVI/A and B images, which includes the pixel numbers $(i_0, j_0)$ of the Sun center in the images (CRPIX1, CRPIX2), the pixel sizes $(\Delta x, \Delta y)$ in arcseconds (CDELT1, CDELT2), the solar radius $R_\odot$ in arcseconds (RSUN), the position angle $P$ (in degrees, or $p = P(\pi/180)$ in radian) of solar North in the image (CROTA), and the heliographic longitude $[l_0]$ and latitude $[b_0]$ of the subsolar point of the STEREO spacecraft in a Stonyhurst coordinate system seen from Earth (HGLON, HGLAT). The solar radius in units of image pixels is then $r_\odot = R_\odot/\Delta x \approx R_\odot/\Delta y$. The $(X_{\mathrm{sc}}, Y_{\mathrm{sc}})$ coordinates of a pixel location $(i, j)$ in a EUVI image are then with respect to Sun center in units of solar radii,

$$X_{\mathrm{sc}} = (i - i_0)/r_\odot,$$
$$Y_{\mathrm{sc}} = (j - j_0)/r_\odot, \tag{3}$$

or rotated by the position angle $[p]$ to a Cartesian spacecraft coordinate system with the *y-axis* aligned with solar North,

$$x_{\mathrm{sc}} = X_{\mathrm{sc}} \cos(p) - Y_{\mathrm{sc}} \sin(p),$$

$$y_{sc} = X_{sc} \sin(p) + Y_{sc} \cos(p), \tag{4}$$

$$z_{sc} = \sqrt{1 - x_{sc}^2 - y_{sc}^2},$$

which provides the longitude $[l_{sc}]$ and latitude $[b_{sc}]$ in a spacecraft Stonyhurst coordinate system:

$$b_{sc} = \arcsin(y_{sc}),$$

$$l_{sc} = \arcsin(x_{sc}/\cos[b_{sc}]). \tag{5}$$

The Stonyhurst coordinates $[l, b]$ in an Earth-centered coordinate system with the *y-axis* aligned with solar North is given by the following coordinate transformation, using the heliographic coordinates $[l_0, b_0]$ of the spacecraft suborbital point (Equation (12) in Thompson, 2006):

$$b = \arcsin(y_{sc} \cos b_0 + z_{sc} \sin b_0) = (b_0 + b_{sc}),$$

$$l = l_0 + \arctan\left(x_{sc}\left[z_{sc} \cos(b_0) - y_{sc} \sin(b_0)\right]^{-1}\right) \approx (l_0 + l_{sc}). \tag{6}$$

We provide the spacecraft suborbital coordinates $[l_0, b_0]$, the spacecraft heliographic coordinates $[l_{sc}, b_{sc}]$ of the flare locations, and the Earth-based heliographic coordinates $[l, b]$ of the flare locations in the electronically available STEREO/EUVI event catalog for easy coordinate transformations (*e.g.* to coalign with *Hinode* or SDO). Further information on coordinate systems used for the STEREO/SECCHI instrument suite has been given by Thompson (2006, 2010) and Thompson and Wei (2010).

### 3.3. STEREO/EUVI Event Catalog Information

The mission-long STEREO/EUVI event catalog, generated by reading the entire EUVI database and by application of the previously described automated flare-event detection algorithm, is available at secchi.lmsal.com/EUVI/euvi_autodetection/euvi_events.txt. Here we describe briefly the definitions of the parameters that are listed in this catalog. An extract of one day (8 June 2007) of the catalog is listed in Table 1, with a graphical representation shown in Figure 2. The flare catalog can also be read by the IDL routine SEC-CHI_EUVI_FLARECAT in the SolarSoftWare (SSW).

The Table 1 includes the year, month, and day of observations (columns 1 – 3), the flare EUV peak time $[t_p]$ is given in hours and minutes (columns 4 – 5), the cadence $[t_c]$ during the event, which is different for each wavelength and spacecraft, is given in units of minutes (column 6), the spacecraft (A) or (B) where the flare event is detected (column 7), a successive event numbering per day and spacecraft (column 8), the wavelengths [171, 195, 284, or 304 Å] (column 9), the flare-background flux $[f_{b1}]$ in units of [DN s$^{-1}$] as defined in Figure 2 (column 10), the flare-related flux enhancement $[df = (f_p - f_{b1})]$ above the background (column 11), the background flux change $[db = (f_{b2} - f_{b1})]$ during the event (column 12), the (time-integrated) fluence $[F]$ during the time interval $[t_{b1}, t_{b2}]$ in units of [$10^3$ DN] (column 13), the rise time $[t_r = (t_p - t_{b1})]$ (column 14), the decay time $[t_d = (t_{b2} - t_p)]$ (column 15), the time delay of the next GOES flare peak $[t_g = (t_p^{GOES} - t_p^{EUVI})]$ in units of minutes, within an interval of $[\Delta t = 0.5$ hour] (column 16), and the preflare-background-subtracted GOES class (column 17). The GOES class may be smaller than the NOAA classification in the case of weak flares, if the preflare-background level is elevated. In the absence of any near-simultaneous GOES flare, a default GOES class of Z0.0 and delay of 99 is displayed for easier machine readability. Further we list the spacecraft suborbital coordinates $[l_0, b_0]$

**Table 1** Extract from the STEREO/EUVI catalog 2006–2012 for 8 June 2007, containing the date [year, month, day] and the peak time [$t_p$] (hours, minutes), the time cadence [$t_c$] (min), the spacecraft [A, B], a daily event number per spacecraft [#], the wavelength [$\lambda$ [Å]], the preflare-background flux [$f_{b1}$ [DN s$^{-1}$]], the peak flux [d$f = (f_p - f_{b1})$] [DN s$^{-1}$], the background change [d$b = (f_{b2} - f_{b1})$] [DN s$^{-1}$], the fluence [$F$] [$10^3$ DN], the rise time [$t_r = (t_p - t_{b1})$] [minutes], the decay time [$t_d = (t_{b2} - t_p)$] (minutes), the GOES peak time difference [$t_g = (t_{GOES} - t_p)$] (minutes), the GOES class (G), the spacecraft suborbital longitude [$l_0$] and latitude [$b_0$], the spacecraft heliographic coordinates of the event [$l_{sc}, b_{sc}$], the Earth-based heliographic coordinates [$l, b$] of the event, and the distance from Sun center seen from Earth [$r$], see description in Section 3.3.

| Date | $t_p$ | $t_c$ | sc | # | $\lambda$ | $f_{b1}$ | d$f$ | d$b$ | $F$ | $t_r$ | $t_d$ | $t_g$ | G | $l_0$ | $b_0$ | $l_{sc}$ | $b_{sc}$ | $l$ | $b$ | $r$ |
|---|---|---|---|---|---|---|---|---|---|---|---|---|---|---|---|---|---|---|---|---|
| 2007 6 8 | 1:35 | 7 | A | 1 | 195 | 364.2 | 33.0 | 26.9 | 10 | 29 | 10 | 0 | C1.7 | 7 | 1 | −7 | −6 | 0 | −5 | 0.179 |
| 2007 6 8 | 1:36 | 4 | A | 2 | 171 | 685.3 | 49.8 | 26.2 | 24 | 29 | 7 | 0 | C1.7 | 7 | 1 | −7 | −12 | 0 | −11 | 0.250 |
| 2007 6 8 | 1:36 | 9 | A | 3 | 304 | 1545.0 | 630.7 | 226.0 | 358 | 20 | 19 | 0 | C1.7 | 7 | 1 | −7 | −6 | 0 | −5 | 0.179 |
| 2007 6 8 | 1:36 | 7 | B | 1 | 195 | 337.1 | 22.7 | 17.7 | 8 | 20 | 10 | 0 | C1.7 | −4 | 0 | 3 | −5 | 0 | −6 | 0.113 |
| 2007 6 8 | 1:36 | 7 | B | 2 | 171 | 579.7 | 61.3 | 19.7 | 38 | 22 | 29 | 0 | C1.7 | −4 | 0 | 3 | −5 | 0 | −6 | 0.113 |
| 2007 6 8 | 1:37 | 10 | B | 3 | 304 | 1479.0 | 566.8 | 184.8 | 327 | 20 | 20 | 0 | C1.7 | −4 | 0 | 3 | −5 | 0 | −6 | 0.113 |
| 2007 6 8 | 1:46 | 19 | A | 4 | 284 | 154.4 | 14.8 | 8.5 | 12 | 20 | 19 | 6 | B4.8 | 7 | 1 | −7 | −6 | 0 | −5 | 0.179 |
| 2007 6 8 | 1:47 | 20 | B | 4 | 284 | 139.4 | 11.7 | 6.6 | 10 | 20 | 20 | 5 | B4.8 | −4 | 0 | 3 | −5 | 0 | −6 | 0.113 |
| 2007 6 8 | 1:51 | 7 | B | 5 | 171 | 586.0 | 27.0 | 13.3 | 41 | 22 | 22 | 1 | B4.8 | −4 | 0 | 3 | −5 | 0 | −6 | 0.113 |
| 2007 6 8 | 1:55 | 9 | A | 5 | 195 | 372.0 | 22.3 | 14.5 | 37 | 29 | 30 | −2 | B4.8 | 7 | 1 | −7 | −6 | 0 | −5 | 0.179 |
| 2007 6 8 | 4:26 | 7 | A | 6 | 304 | 1658.3 | 234.2 | 67.6 | 167 | 19 | 20 | −7 | C2.4 | 7 | 1 | −1 | −11 | 6 | −10 | 0.206 |
| 2007 6 8 | 4:27 | 9 | B | 6 | 304 | 1538.0 | 196.9 | 52.0 | 156 | 19 | 20 | −8 | C2.4 | −4 | 0 | 11 | −10 | 6 | −11 | 0.268 |
| 2007 6 8 | 5:06 | 6 | A | 7 | 304 | 1725.9 | 179.2 | −16.3 | 130 | 19 | 19 | −6 | C1.4 | 7 | 1 | −1 | −11 | 6 | −10 | 0.206 |
| 2007 6 8 | 5:07 | 10 | B | 7 | 304 | 1590.0 | 152.8 | −25.3 | 140 | 20 | 20 | −7 | C1.4 | −4 | 0 | 11 | −10 | 6 | −11 | 0.268 |
| 2007 6 8 | 7:56 | 9 | A | 8 | 304 | 1774.4 | 135.0 | 32.5 | 197 | 29 | 19 | −2 | B2.7 | 7 | 1 | −1 | −11 | 6 | −10 | 0.206 |
| 2007 6 8 | 7:57 | 9 | B | 8 | 304 | 1635.0 | 63.5 | −26.2 | 101 | 19 | 20 | −3 | B2.7 | −4 | 0 | 51 | −11 | 47 | −12 | 0.793 |
| 2007 6 8 | 8:36 | 5 | A | 9 | 171 | 761.2 | 22.1 | −50.5 | 32 | 15 | 22 | −2 | C3.2 | 7 | 1 | −1 | −11 | 6 | −10 | 0.206 |
| 2007 6 8 | 8:36 | 10 | A | 10 | 304 | 1806.9 | 548.6 | 206.4 | 617 | 20 | 29 | −2 | C3.2 | 7 | 1 | 4 | −11 | 12 | −9 | 0.208 |
| 2007 6 8 | 8:36 | 10 | B | 9 | 195 | 393.8 | 11.2 | −1.7 | 13 | 30 | 20 | −3 | C3.2 | −4 | 0 | 11 | −10 | 6 | −11 | 0.268 |
| 2007 6 8 | 8:36 | 6 | B | 10 | 171 | 617.7 | 17.6 | −35.3 | 33 | 15 | 22 | −3 | C3.2 | −4 | 0 | 11 | −10 | 6 | −11 | 0.268 |

**Table 1** (*Continued.*)

| Date | $t_p$ | $t_c$ | sc | # | $\lambda$ | $f_{b1}$ | $df$ | $db$ | $F$ | $t_r$ | $t_d$ | $t_g$ | $G$ | $l_0$ | $b_0$ | $l_{sc}$ | $b_{sc}$ | $l$ | $b$ | $r$ |
|---|---|---|---|---|---|---|---|---|---|---|---|---|---|---|---|---|---|---|---|---|
| 2007 6 8 | 8:37 | 8 | B | 11 | 304 | 1608.8 | 458.3 | 235.7 | 246 | 20 | 20 | −3 | C3.2 | −4 | 0 | 16 | −3 | 12 | −3 | 0.287 |
| 2007 6 8 | 9:06 | 20 | A | 11 | 284 | 189.7 | 13.7 | 10.4 | 10 | 20 | 19 | −20 | C3.3 | 7 | 1 | 4 | −11 | 12 | −9 | 0.208 |
| 2007 6 8 | 9:07 | 20 | B | 12 | 284 | 159.2 | 9.6 | 7.7 | 6 | 20 | 20 | −21 | C3.3 | −4 | 0 | 11 | −10 | 6 | −11 | 0.268 |
| 2007 6 8 | 9:21 | 6 | A | 12 | 171 | 710.7 | 21.3 | −7.1 | 37 | 22 | 22 | 99 | Z0.0 | 7 | 1 | 4 | −11 | 12 | −9 | 0.208 |
| 2007 6 8 | 12:13 | 4 | A | 13 | 171 | 729.8 | 59.4 | 43.3 | 52 | 30 | 7 | −2 | B5.2 | 7 | 1 | 0 | −17 | 7 | −16 | 0.306 |
| 2007 6 8 | 12:14 | 6 | B | 13 | 171 | 586.8 | 28.4 | 14.4 | 28 | 22 | 15 | −3 | B5.2 | −4 | 0 | 11 | −10 | 6 | −11 | 0.268 |
| 2007 6 8 | 12:36 | 9 | A | 14 | 304 | 1837.7 | 93.3 | 46.4 | 98 | 29 | 30 | 0 | B7.9 | 7 | 1 | −1 | −11 | 6 | −10 | 0.206 |
| 2007 6 8 | 12:37 | 7 | B | 14 | 304 | 1640.4 | 69.3 | 21.1 | 54 | 9 | 20 | −1 | B7.9 | −4 | 0 | 11 | −10 | 6 | −11 | 0.268 |
| 2007 6 8 | 13:36 | 7 | A | 15 | 304 | 1854.3 | 113.1 | 3.4 | 85 | 9 | 29 | 0 | B3.3 | 7 | 1 | 4 | −11 | 12 | −9 | 0.208 |
| 2007 6 8 | 13:37 | 7 | B | 15 | 304 | 1622.6 | 97.4 | 11.6 | 55 | 10 | 20 | 0 | B3.3 | −4 | 0 | 17 | −9 | 13 | −10 | 0.345 |
| 2007 6 8 | 14:46 | 10 | A | 16 | 304 | 2014.3 | 160.0 | −19.8 | 324 | 30 | 20 | 99 | Z0.0 | 7 | 1 | 4 | −11 | 12 | −9 | 0.208 |
| 2007 6 8 | 14:47 | 10 | B | 16 | 304 | 1836.1 | 28.4 | −109.8 | 114 | 20 | 20 | 99 | Z0.0 | −4 | 0 | 17 | −9 | 13 | −10 | 0.345 |
| 2007 6 8 | 15:06 | 20 | A | 17 | 284 | 204.3 | 9.6 | −2.2 | 12 | 20 | 19 | 99 | Z0.0 | 7 | 1 | 4 | −11 | 12 | −9 | 0.208 |
| 2007 6 8 | 15:07 | 20 | B | 17 | 284 | 167.8 | 8.0 | −0.4 | 9 | 20 | 19 | 99 | Z0.0 | −4 | 0 | 17 | −9 | 13 | −10 | 0.345 |
| 2007 6 8 | 17:06 | 5 | A | 18 | 304 | 1800.1 | 89.7 | 61.0 | 26 | 9 | 20 | −1 | B5.1 | 7 | 1 | 4 | −11 | 12 | −9 | 0.208 |
| 2007 6 8 | 17:07 | 6 | B | 18 | 304 | 1579.8 | 74.5 | 47.5 | 22 | 9 | 20 | −2 | B5.1 | −4 | 0 | 17 | −9 | 13 | −10 | 0.345 |
| 2007 6 8 | 17:26 | 19 | A | 19 | 284 | 194.5 | 10.8 | 8.4 | 7 | 19 | 20 | −21 | B5.1 | 7 | 1 | 4 | −11 | 12 | −9 | 0.208 |
| 2007 6 8 | 17:27 | 19 | B | 19 | 284 | 163.4 | 8.9 | 7.2 | 6 | 19 | 20 | −22 | B5.1 | −4 | 0 | 17 | −9 | 13 | −10 | 0.345 |
| 2007 6 8 | 18:56 | 7 | A | 20 | 304 | 1766.4 | 118.2 | 56.6 | 56 | 19 | 20 | −4 | B4.8 | 7 | 1 | 10 | −10 | 18 | −8 | 0.254 |
| 2007 6 8 | 22:58 | 6 | A | 21 | 171 | 848.0 | 16.3 | −22.4 | 41 | 22 | 30 | −6 | B1.4 | 7 | 1 | 0 | −17 | 7 | −16 | 0.306 |
| 2007 6 8 | 23:26 | 8 | A | 22 | 304 | 1728.5 | 36.5 | −93.8 | 94 | 20 | 30 | −3 | B2.3 | 7 | 1 | 10 | −10 | 18 | −8 | 0.254 |
| 2007 6 8 | 23:27 | 10 | B | 20 | 304 | 1561.1 | 42.7 | −58.5 | 69 | 20 | 30 | −4 | B2.3 | −4 | 0 | 17 | −9 | 13 | −10 | 0.345 |
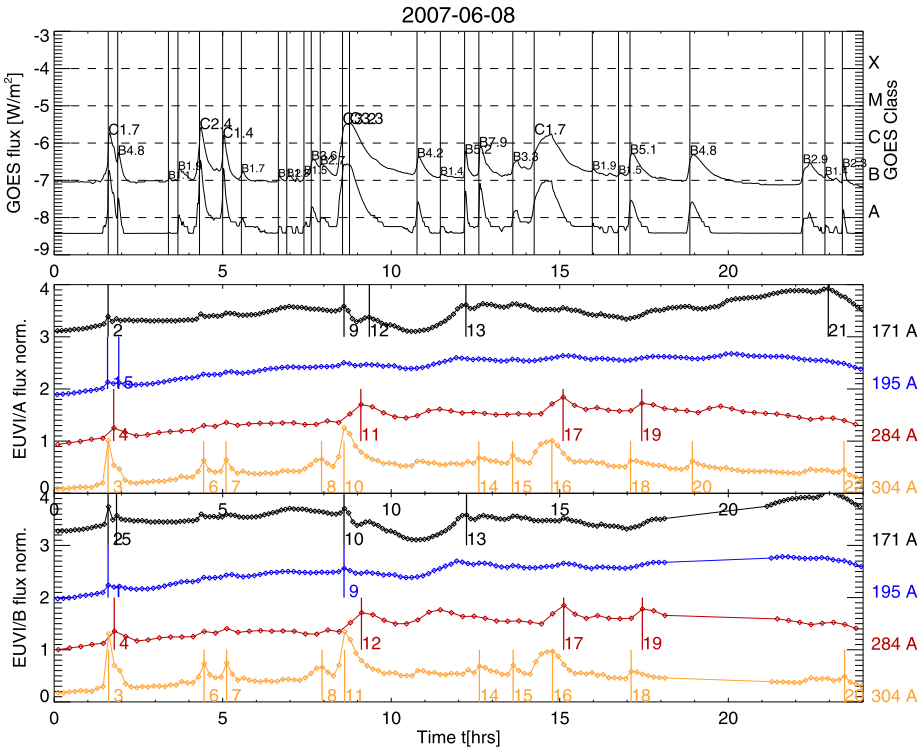
**Figure 2** Example of automated EUVI event detection on 8 June 2007, showing the GOES light curves with automatically detected GOES flares (top panel), the four EUV temporal profiles (added from the ten macropixels with the largest daily fluxes) in 171, 195, 284, and 304 Å with detected EUVI events from spacecraft STEREO-A (second frame) and STEREO-B (third frame). Each color corresponds to a different wavelength filter. The EUV fluxes are incrementally shifted and normalized by $\pm 5$ standard deviations. The parameters of each event detected on this day are also listed in Table 1.

(columns 18 – 19), the flare location $[l_{sc}, b_{sc}]$ in spacecraft Stonyhurst coordinates (Equation (5)) (column 20 – 21), the flare location $[l, b]$ in Earth-based Stonyhurst coordinates (Equation (6)) (columns 22 – 23), and the distance $[r]$ of the flare location from Sun center in the EUVI image (column 24). The STEREO/EUVI event catalog is chronologically ordered, containing the eight merged subcatalogs of flare events independently detected by the two spacecraft [A, B] and by the four wavelength filters [171, 195, 284, 304 Å]. Thus, some flare events may have up to eight near-simultaneous detections in this catalog, where the peak times differ slightly because of the different cadences in each wavelength filter.

## 4. STEREO/EUVI Event Statistics

Statistics of detected EUVI events are given in Table 2, showing the number of events detected in every year from 2006 to 2012, and sorted by wavelengths (171, 194, 284, 304 Å) and spacecraft (STEREO-A, B). The total number of detected events with both spacecraft in all four wavelength filters amounts to some $\approx 20\,000$ events, where 79 % of all EUVI event

**Table 2** Statistics of detected EUVI events, sampled per year (rows), spacecraft (A, B) and wavelengths (171, 195, 284, 304 Å; columns).

| Year | A 171 | A 195 | A 284 | A 304 | B 171 | B 195 | B 284 | B 304 | Sum |
|------|-------|-------|-------|-------|-------|-------|-------|-------|-----|
| 2006 | 11    | 14    | 6     | 8     | 2     | 6     | 5     | 21    | 73  |
| 2007 | 148   | 101   | 215   | 589   | 124   | 89    | 190   | 507   | 1963 |
| 2008 | 35    | 43    | 221   | 350   | 19    | 22    | 168   | 238   | 1096 |
| 2009 | 38    | 68    | 172   | 559   | 29    | 58    | 168   | 361   | 1453 |
| 2010 | 70    | 216   | 39    | 1352  | 18    | 147   | 19    | 1077  | 2938 |
| 2011 | 108   | 325   | 52    | 2823  | 81    | 210   | 47    | 2470  | 6116 |
| 2012 | 71    | 387   | 60    | 2880  | 66    | 261   | 55    | 2557  | 6337 |
| Sum  | 481   | 1154  | 765   | 8561  | 339   | 793   | 652   | 7231  | 19976 |
|      | 2.4 % | 5.8 % | 3.8 % | 42.9 % | 1.7 % | 4.0 % | 3.3 % | 36.2 % | 100 % |

detections are detected in 304 Å, 10 % in 195 Å, 7 % in 284 Å, and 4 % in 171 Å. The summation in the channels demonstrate that most events were detected in the 304 Å channel. Substantially fewer events are detected in the other three channels, partially because of the EUV dimming at the onset of a CME which can suppress the impulsive EUV increase at the onset of a flare, and partially because of the longer cadences used at various times in the 171, 195, and 284 Å channels. Our algorithm requires a minimum cadence of $t_c \leq 0.5$ hour for reliable detection of impulsive flux increases, and thus channels with longer cadences are not capable of event detection. The summations for each year reflect the variability of the solar cycle, which exhibited an extended minimum during the years 2008 – 2009, and produced about ten times more EUV events during the solar maximum years of 2011 – 2012.

### 4.1. Event Detection Rates EUVI *Versus* GOES

The number of detected EUVI events is presented as histograms in Figure 3, for each spacecraft [STEREO-A and -B] and wavelength [171, 195, 284, 304 Å] separately. For comparison, the monthly event detection rate of GOES 1 – 8 Å flares is also shown (Figure 3, bottom), based on the automated detection algorithm used by Aschwanden and Freeland (2012). These histograms demonstrate that:

 i)  the number of detected events in EUV and soft X-rays is almost proportional for the 304 Å channel,
 ii) both the EUV 304 Å and soft X-rays 1 – 8 Å detection rate show a similar modulation through the solar cycle, and
iii) the EUV detection rates are similar for both spacecraft STEREO-A and -B.

These detection rates reveal for the first time with large statistics that flare detection in EUV wavelengths can be as efficient as in soft X-rays. It is often stated that flare-event detection in the EUV is hampered by the effects of EUV dimming, which partially explains that we detect a smaller fraction of events in 171 and 195 Å, but a fair comparison can only be made with equal cadences. During the STEREO mission, the 171 and 304 Å channels were operated with a relatively high cadence during the first years of the mission, while 195 and 304 Å channels were operated with a relatively high cadence during the later years of the mission. The 304 Å channel, which is sensitive to chromospheric temperatures, appears
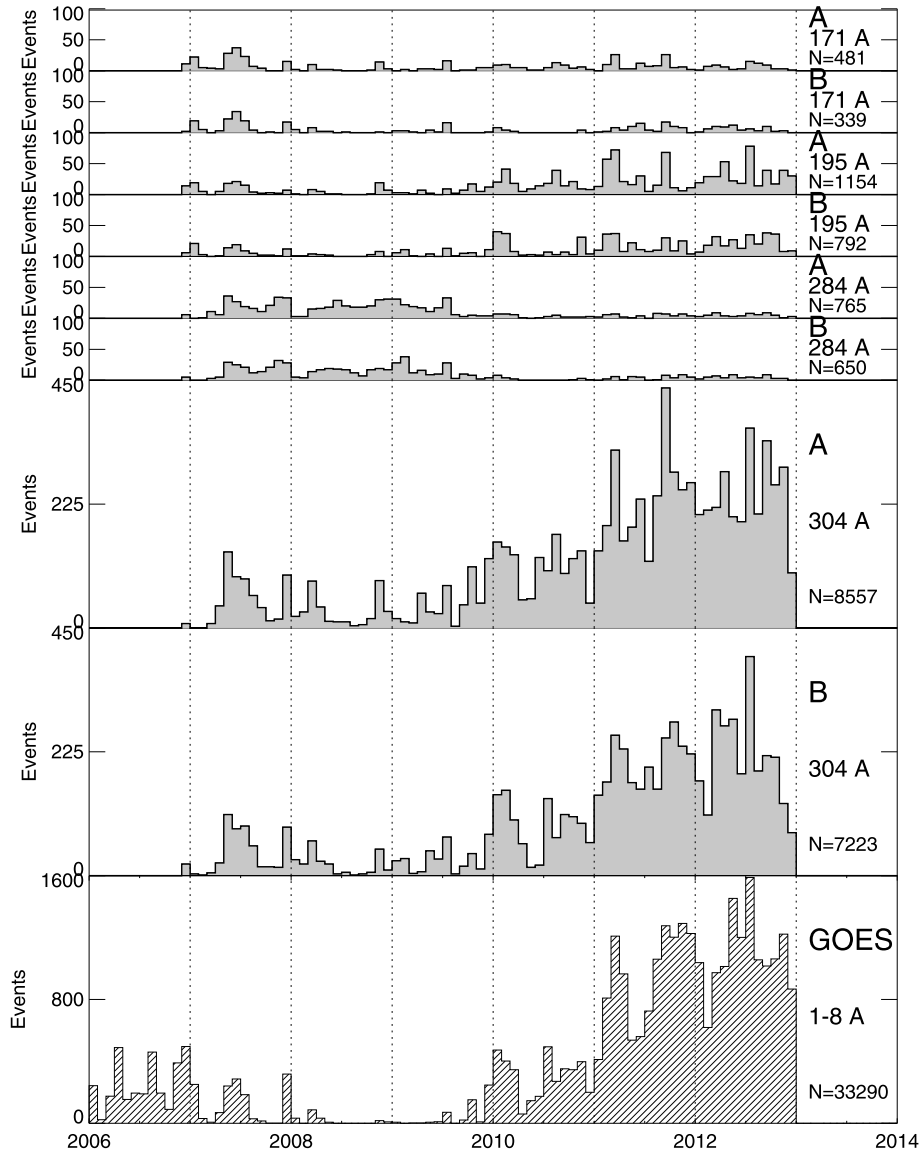
**Figure 3** Monthly detection rate of EUVI/A and B events for each wavelength filter [171, 195, 284, 304 Å], and comparison with the detection rate of GOES events (Aschwanden and Freeland, 2012) in bottom panel.

to be the most suitable channel for EUV event detection, even at times when the cadences were similar in the other channels.

In Figure 4 we explicitly show the near-proportionality of the (monthly) detection rate of the 304 Å channel of EUVI/A and B with the (monthly) detection rate of the GOES 1–8 Å channel. The ratio of events detected with GOES 1–8 Å (with the algorithm of Aschwanden and Freeland, 2012) and those detected in EUVI 304 Å is a factor or ≈ 4.4 (diagonal line in Figure 4), with a small scatter for months with high solar activity. During months of very low

**Figure 4** Monthly detection rate of EUVI 304 Å events *versus* the GOES 1 – 8 Å events. The diagonal line indicates a proportional detection ratio of 1 EUV event to 4.4 GOES events.
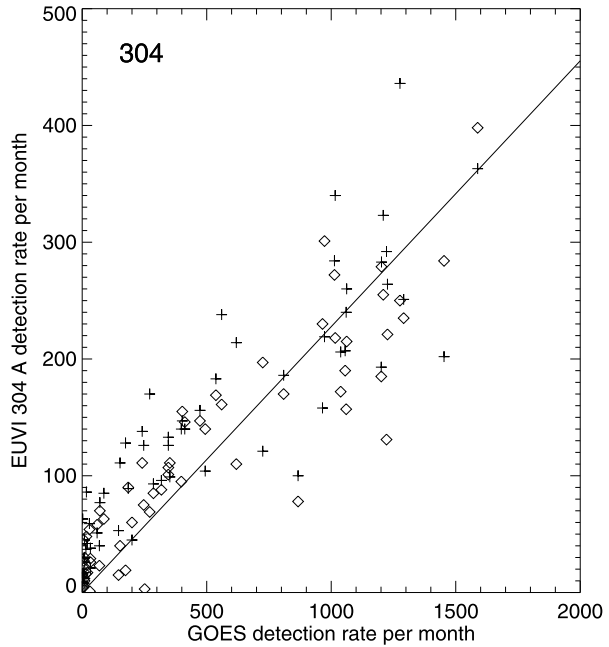


flare rates, such as during the extended solar minimum of 2008 – 2009, the relative scatter is larger.

## 4.2. Size Distribution of EUV Peak Fluxes

The size distributions of the (automatically detected) background-subtracted EUV flux enhancements [$df = (f_p - f_b)$] are shown in the form of log–log histograms in Figure 5, separately for the spacecraft STEREO-A and -B (left and right panels) and for the four EUVI wavelengths. Regardless of the spacecraft and wavelength, all eight size distributions have a similar power-law slope, with a mean and standard deviation of $\alpha_P^{obs} = 2.5 \pm 0.2$. This value is similar to a sample of 155 M- and X-class flare events observed with SDO/AIA in seven (mostly coronal) wavelengths, for which an average power-law slope of $\alpha_P = 2.1 \pm 0.1$ was found (Aschwanden and Shimizu, 2013). The small difference in the slope may be explained by different detection algorithms and detection criteria (background flux, flux threshold, time interval).

## 4.3. Size Distribution of EUV Event Durations

The temporal parameters that we measured for each event consist of the preflare flux-minimum time [$t_{b1}$], the peak time [$t_p$], and the postflare flux-minimum time [$t_{b2}$], bound by a maximum time interval of [$t_p \pm 0.5$ hour]. From these three time points we can define a rise time [$t_r = (t_p - t_{b1})$], and a lower limit of the decay time [$t_d = (t_{b2} - t_p)$], if the background decreases with time [$db = (f_{b2} - f_{b1}) < 0$]. For increasing background fluxes, however, a more realistic decay time can be extrapolated by assuming an exponential-decay function and using the flux [$f_p$] at the peak time [$t_p$] and the flux [$f_{b2}$] at $t_{b2}$ as constraints to calculate the e-folding decay time [$\tau_e$], and the end time [$t_e$] when the exponentially decaying flux reaches a lower limit of $q_e = f_e/f_p$, say $\approx 10\%$ of the peak flux [$f_p$] (Figure 1).
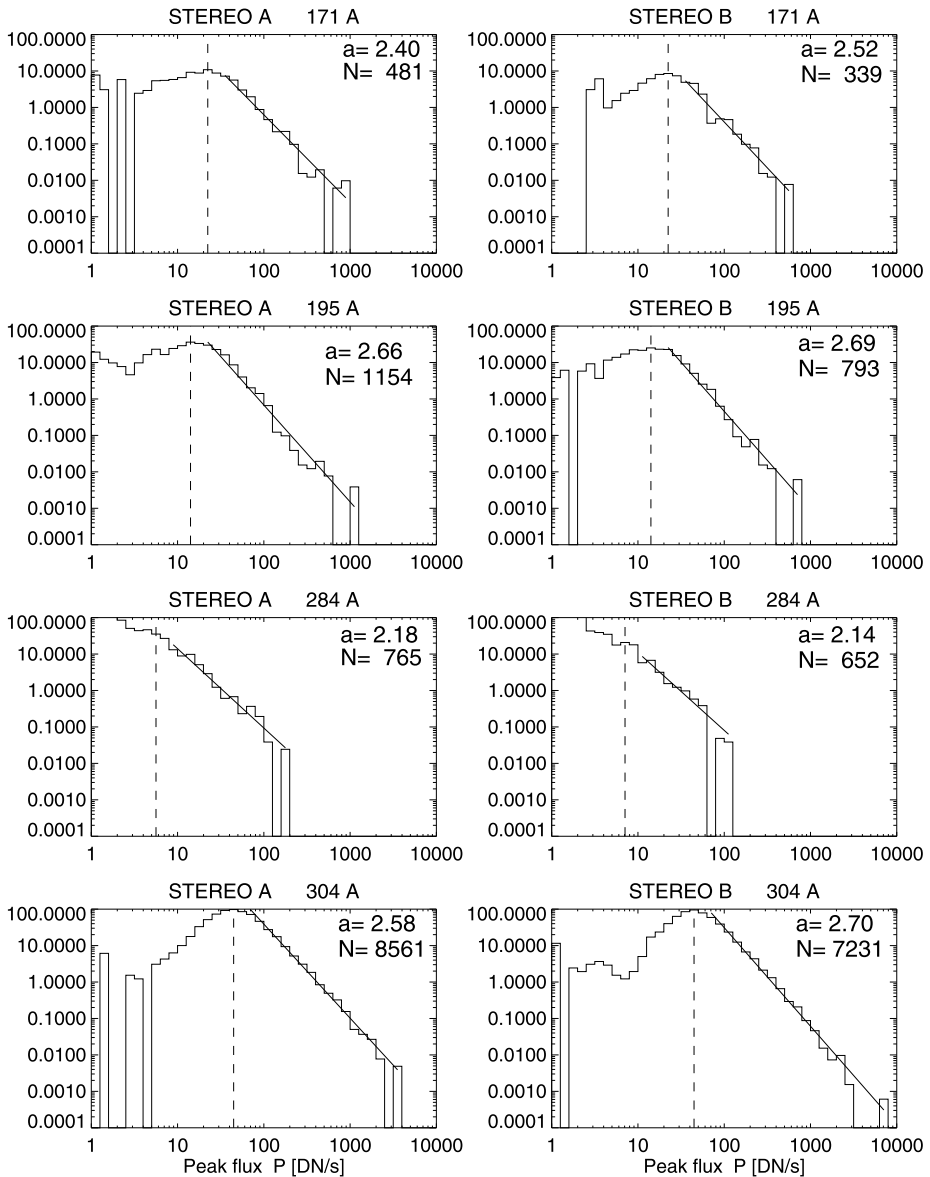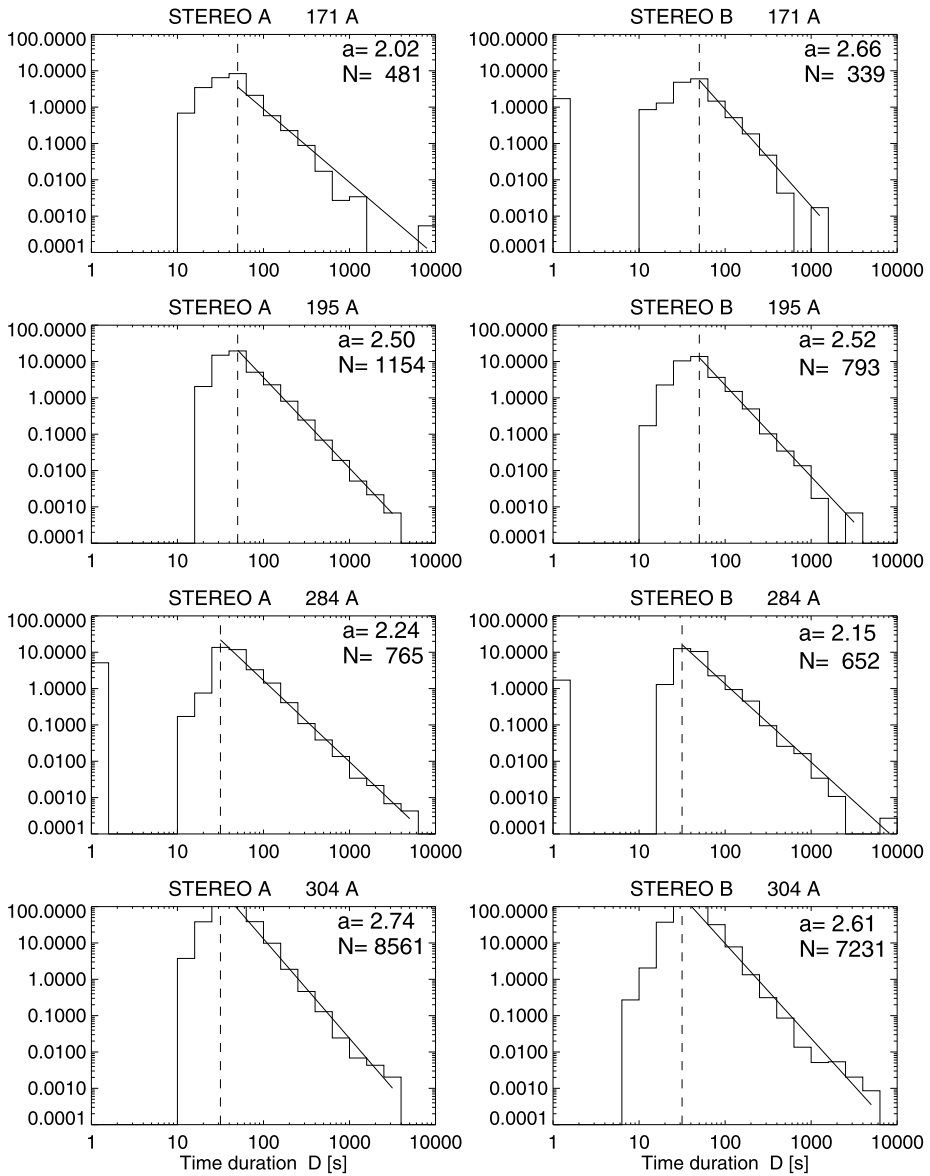
**Figure 5** Size distributions of EUV event peak fluxes [$P$], for each spacecraft STEREO-A and -B (columns) and four wavelength channels (rows). Power-law fits are indicated with their slopes [$\alpha_P$].

Thus we have the relationships

$$\frac{(f_{b2} - f_{b1})}{(f_p - f_{b1})} = \exp\left(-\frac{(t_{b2} - t_p)}{\tau_e}\right), \tag{7}$$

$$q_e = \frac{(f_e - f_{b1})}{(f_p - f_{b1})} = \exp\left(-\frac{(t_e - t_p)}{\tau_e}\right), \tag{8}$$

**Figure 6** Size distributions of EUV event durations [$\tau$], for each spacecraft STEREO-A and -B (columns) and four wavelength channels (rows). Power-law fits are indicated with their slopes [$\alpha_\tau$].

from which the e-folding decay time [$\tau_e$] and the decay time [$t_d = (t_e - t_p)$] can be retrieved. Using this definition of the decay time [$t_d$] we can then define an event duration from the sum of the rise time and decay time [$\tau = t_r + t_d$]. The size distribution of EUV event durations is shown in Figure 6. The average power-law slope is $\alpha_\tau = 2.3 \pm 0.3$.

## 4.4. Self-organized Criticality Model

A theoretical model of a slowly driven fractal-diffusive self-organized criticality system (FD-SOC: Aschwanden, 2012, 2013) predicts the following:

i) A power-law length scale distribution $[N(L)]$ that is reciprocal to the Euclidean volume $[V = L^S]$, with Euclidean dimension $[S]$, postulated by the scale-free probability conjecture

$$N(L) \propto L^{-S}. \tag{9}$$

ii) A diffusion-type relationship (with diffusion index $[\beta = 1]$ for classical diffusion or random walk) between spatial $[(L)]$ and temporal $[T]$ scales

$$L \propto T^{\beta/2}. \tag{10}$$

iii) A fractal geometry for SOC avalanche volumes $[V]$

$$V \propto L^{D_S}, \quad D_S \approx \frac{(1+S)}{2}. \tag{11}$$

iv) Characterization of the flux–volume relationship between the observed flux $[F]$ in a given wavelength and the emitting volume $[V]$ with an additional power-law relationship with index $\gamma$

$$F \propto V^\gamma. \tag{12}$$

Based on these four basic assumptions, the following power-law indices $[\alpha_x]$ are predicted for the length scales $[L]$, volumes $[V]$, time durations $[T]$, time-averaged fluxes $[F]$, and peak fluxes $[P]$:

$$\alpha_L = S, \tag{13}$$

$$\alpha_V = 1 + (S - 1)/D_S, \tag{14}$$

$$\alpha_T = 1 + (S - 1)\beta/2, \tag{15}$$

$$\alpha_F = 1 + (S - 1)/(\gamma D_S), \tag{16}$$

$$\alpha_P = 1 + (S - 1)/(\gamma S). \tag{17}$$

Thus, if we set the Euclidean dimension to $S = 3$ we expect a mean fractal (Hausdorff) dimension of $D_3 = (1 + S)/2 = 2.0$, a volume power-law index of $\alpha_V = 2$, a duration power-law index of $\alpha_T = 1 + \beta$, and a peak flux power-law index of $\alpha_P = 1 + 2/(3\gamma)$. In the special case of classical diffusion we expect $\beta = 1$ and $\alpha_T = 2.0$. The observed time duration power-law slope of $\alpha_T = 2.4 \pm 0.3$ is close to the expected value for classical diffusion. For comparison, a power-law slope of $\alpha_T = 2.02 \pm 0.04$ was found for GOES flares (Aschwanden and Freeland, 2012).

If we take the observed peak-flux power-law slope of $\alpha_P = 2.5 \pm 0.2$ at face value, we infer a flux–volume power-law index of $\gamma \approx 0.45$. In comparison, very similar flux–volume power-law indices of $\gamma = 0.42 \pm 0.16$ were found for a data set of 155 M- and X-class flare analyzed in the eight AIA wavelengths (Figure 4 in Aschwanden and Shimizu, 2013). Thus our EUV event detection algorithm seems to yield flux distributions that are fully consistent with other statistical studies of EUV events.

4.5. STEREO/EUVI *vs.* GOES Flux Correlations

Since we identified a large number of time-coincident events in EUV and soft X-rays, we can also quantify the flux–flux relationship between EUV events and soft X-ray events. We find that the 284 Å flux correlates best with the GOES 1–8 Å flux (with a cross-correlation coefficient of ccc $\approx 0.5$), which is sensitive to a temperature range of $\approx 2.0$ MK that is closest to the GOES 1–8 Å channel. The events detected in 171 and 195 Å are probably less correlated due to the EUV dimming effects, which reduce the EUV flux at the beginning of flares during the launch of a CME, and causes a mass loss in the flaring part of the corona. We show a scatterplot of the EUVI fluxes with the GOES 1–8 Å flux in Figure 7. A linear regression fit with the ordinary least-squares bisector method (Isobe *et al.*, 1990) yields a relationship of

$$f_{\text{EUVI}} \propto (f_{\text{GOES}})^{0.72 \pm 0.05}. \tag{18}$$

In another recent study of flares simultaneously observed with STEREO/EUVI and GOES, the 195 Å flux was found to exhibit a good correlation with the GOES flux, which was expected due to the Fe XXIV line in the 195 Å response function that has a sensitivity to hot plasma with a temperature of $\approx 20$ MK, similar to the response of the GOES 1–8 Å channel (Nitta *et al.*, 2013). If we mimic a similar selection of large flares with a brightness above the GOES C2-class level, we indeed find also a better correlation of the 195 Å flux with the GOES 1–8 Å flux (ccc $= 0.50$) than the 284 Å flux (ccc $= 0.34$). Thus, the overall correlation behavior between EUV and soft X-ray fluxes depends on both the observed wavelength and the flux threshold used in the event selection, but generally tends to correlate better for large events.

4.6. Positional Accuracy of Event Locations

Based on our spatial-localization algorithm that uses macropixels with a size of 32 image pixels (or 3.0° heliographic degrees), we expect an uncertainty in the heliographic longitude $[l \pm 3.0°]$ and latitude $[b \pm 3.0°]$ at disk center. The uncertainty increases for sources that are located near the limb, as seen from one of the two spacecraft, which can be estimated from the transformation of the projected longitude to the unprojected longitude. If a source is located at a longitude $[l_{\text{sc}}]$ in the spacecraft view, an uncertainty of $\delta = 3.0°$ projected heliographic degrees translates into an error $[\Delta l]$ of

$$\Delta l \approx \frac{\delta}{\cos l_{\text{sc}}}. \tag{19}$$

Thus for a longitude of $l_{\text{sc}} = 45°, 60°$, or $75°$ heliographic degrees, we expect an uncertainty of $\Delta l \approx 4.2°, 6.0°$, or $11.6°$, limited by a maximum value of $\Delta_{\max} = \arccos(1 - \delta) = 13.2°$ heliographic degrees for positions near the limb, beyond $l_{\text{sc}} \gtrsim (90° - \Delta_{\max}) \approx 76.8°$. Thus, for the chosen macropixel size of 3.0°, in our automated EUV event-detection algorithm we expect a median uncertainty of $\Delta l \approx \pm 4.2°$, the value corresponding to the median longitude of $l_{\text{sc}} = 45°$. This is also comparable with the spatial extent of a flare region.

As an experimental test of the accuracy of EUV event positions given in our EUV event catalog, we compared the listed positions seen from Earth $[l, b]$ with those obtained for a sample of 16 major flares observed with EUVI behind the limb, compiled in Table 1 of Nitta *et al.* (2013), including events previously analyzed by Veronig *et al.* (2010), Dresing *et al.* (2012), Rouillard *et al.* (2012), and Mewaldt *et al.* (2013). For this sample of 16 major flares we find a total of 37 coincident event detections in our EUVI catalog (created
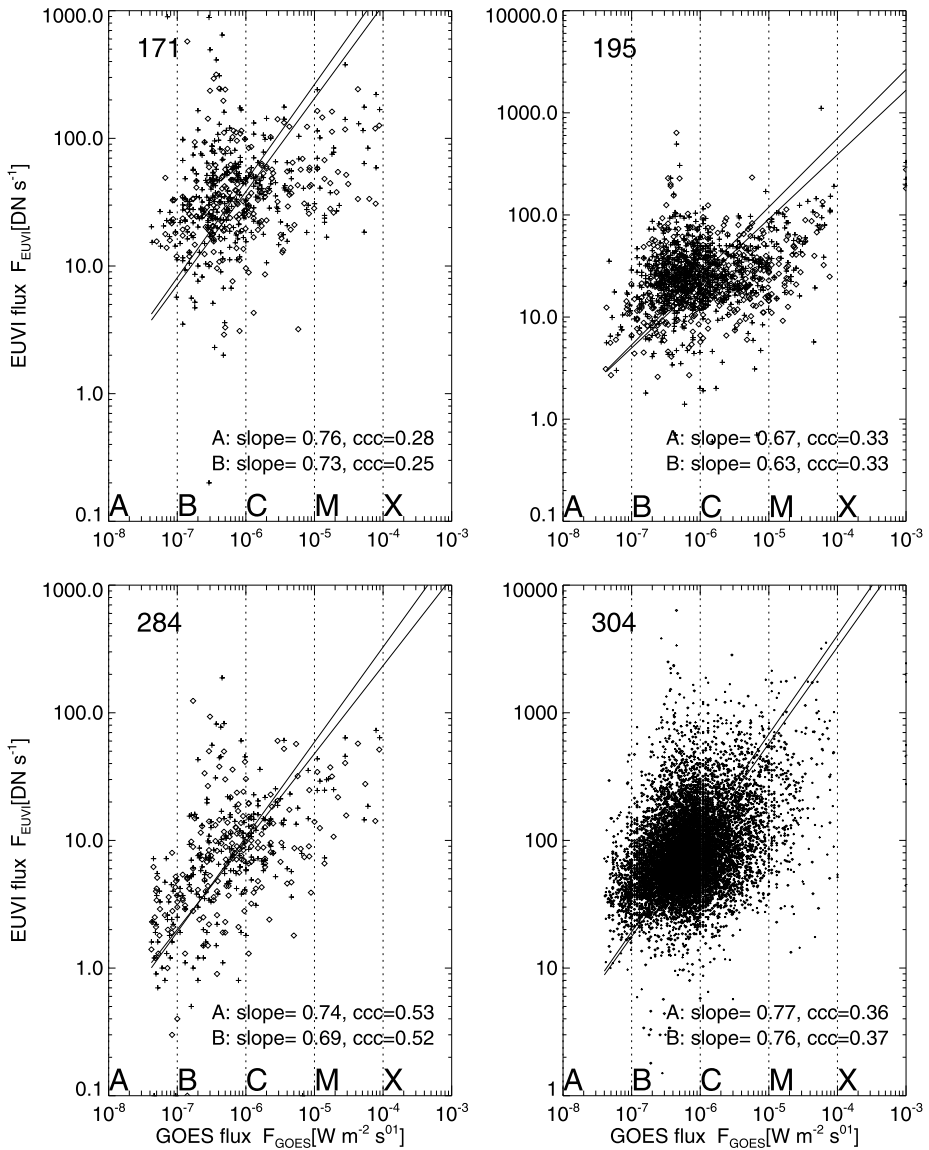
**Figure 7** EUVI fluxes [171, 195, 284, 304 Å] *versus* the GOES flux of all events simultaneously detected with EUVI and GOES. The data from STEREO-A are indicated with cross symbols, from STEREO-B with diamond symbols. Separate fits and linear regression fits for both spacecraft are indicated.

by an automated detection algorithm), counting each detection by the two spacecraft and the four wavelength filters separately. The positional difference between the two flare sets is found to have a mean and standard deviation of $\Delta l = 7.8° \pm 4.0°$, which corresponds approximately to our theoretical estimate with a median value of $\Delta l \approx 4.2°$, given the fact that there is an additional uncertainty of similar magnitude in the definition of the flare position, which is given by the spatial extent of an active region: of the order of a few heliographic degrees.

## 5. Summary and Conclusions

We created an automated event-detection algorithm that measures the peak times, EUV fluxes, and heliographic positions of impulsive EUV events from the STEREO-A and -B spacecraft, and in each of the four EUVI wavelength channels (171, 195, 284, 304 Å) separately. The EUV events in this STEREO/EUVI catalog correspond mostly to solar flares detected also in soft X-rays with the GOES 1 – 8 Å channel, down to a level of about GOES class A5. A fraction of EUV events without GOES detections may possibly be associated with filament and prominence activities. The detection efficiency in the different channels depends strongly on the temporal cadence used, which necessarily drops with the progress of the mission due to the increasing distance of the STEREO spacecraft from Earth and the related reduction of telemetry. The primary wavelengths with high cadence were 171 and 304 Å from 2006 to August 2009, while it was 195 and 304 Å for September 2009 to 2012. In addition, EUV dimming that accompanies the launch of CMEs often prevents the detection of flares in the 171, 195, and 284 Å channels due to the partial canceling of EUV brightening and dimming changes in EUV flux time profiles. Thus, the 304 Å channel turned out to be the most efficient channel for EUV event detections (79 %), while the other channels detect a substantially lower number of EUV events (10 % in 195 Å, 7 % in 284 Å, and 4 % in 171 Å); see Table 2.

The statistics of detected events also strongly varies with the solar cycle. The lowest number of EUV events (1096 detections) occurred in the solar-minimum year 2007, while the highest number (6337 detections) was registered in 2012, which is believed to be close to the maximum of the current Solar Cycle 24. Overall we detected 19 976 events, which includes multiple detections by the two spacecraft and four wavelength channels each. If we try to estimate the number of independent solar EUV events, we can take those from the most efficient channel and spacecraft, which is 8561 EUV events detected with EUVI/A in 304 Å (see Table 2). For comparison, a number of 33 290 independent soft X-ray flare events were detected with the GOES 1 – 8 Å channel with an automated algorithm that is about five times more sensitive than the official NOAA solar-flare list (Aschwanden and Freeland, 2012). Thus the detection ratio of these two automated detection algorithms is $33\,290/8561 \approx 3.9$ (see also Figure 3). The detection rates of flare events in EUV 304 Å and soft X-ray GOES 1 – 8 Å is highly correlated, although the 304 Å emission results from impulsive brightenings in the chromosphere due to flare-induced electron precipitation (producing also hard X-rays), while the soft X-ray emission is mostly believed to be of coronal origin from postflare loops that have been filled with chromospherically heated plasma.

Useful quantitative characterizations of event statistics are size distributions of the measured parameters. We find for the occurrence-frequency distribution of EUV peak fluxes a power-law function with a slope of $\alpha_P = 2.5 \pm 0.2$, averaged from all eight wavelength channels on the two STEREO spacecraft. For the occurrence-frequency distribution of EUV event durations we find a power-law function with a slope of $\alpha_T = 2.3 \pm 0.3$. Interpreting the EUV events as nonlinear energy-dissipation events in a slowly driven fractal-diffusive self-organized criticality model (Bak, Tang, and Wiesenfeld, 1987; Aschwanden, 2012, 2013), the measured power-law indices constrain the spatio–temporal diffusion index [$\beta = (\alpha_T - 1) = 1.3 \pm 0.3$] and the flux–volume power-law index [$\gamma = 2/[3(\alpha_P - 1)] \approx 0.45$]. This result is close to the case of classical diffusion [$\beta = 1$]. The flux–volume relationship [$F \propto V^{0.45}$] deviates significantly from proportionality, as found in another recent EUV study from AIA (Aschwanden and Shimizu, 2013), and thus indicates some nonlinear scaling law between the emitted EUV flux and the flare volume [$V$].

The mission-long STEREO/EUVI event catalog of 2006 – 2012 is available at: secchi.lmsal.com/EUVI/euvi_autodetection/euvi_events.txt. Daily EUVI profiles for both

STEREO spacecraft for each of the four wavelength channels are at secchi.lmsal.com/EUVI/euvi_autodetection/DAILY_EUVI_PROFILES/, synthesized from the most active regions on the solar disk (combining the ten macropixels with the highest EUV fluxes), which have a substantially better signal-to-noise ratio than full-disk EUV time profiles. The EUVI event catalog contains information on the peak times, rise times, decay times, peak fluxes, background fluxes before and after the flare, fluences, and heliographic positions of the spacecraft, the EUV events in spacecraft coordinates, and Earth-based heliographic coordinates. The heliographic positions allow for an approximate localization of flare events within a few heliographic degrees (limited by the 3° size of the macropixels used in the automated-detection algorithm). This catalog may be useful for the study of stereoscopically observed flare events and occulted flares on the farside of the Sun.

# References

Aschwanden, M.J.: 2012, *Astron. Astrophys.* **539**, A2.

Aschwanden, M.J.: 2013, In: Aschwanden, M.J. (ed.) *Self-organized Criticality Systems*, Open Academic Press, Berlin, 439. Chapter 13. www.openacademicpress.de/ojs2/index.php/socs.

Aschwanden, M.J., Freeland, S.L.: 2012, *Astrophys. J.* **754**, 112.

Aschwanden, M.J., Shimizu, T.: 2013, *Astrophys. J.* in press.

Aschwanden, M.J., Wülser, J.P., Nitta, N., Lemen, J.: 2009, *Solar Phys.* **256**, 3. ADS:2009SoPh..256....3A. doi:10.1007/s11207-009-9347-4.

Bak, P., Tang, C., Wiesenfeld, K.: 1987, *Phys. Rev. Lett.* **59**, 381.

Dresing, N., Gomez-Herrero, R., Klassen, A., Heber, B., Karthavukh, Y., Dröge, W.: 2012, *Solar Phys.* **281**, 281.

Howard, R.A., Moses, J.D., Vourlidas, A., Newark, J.S., Socker, D.G., Plunkett, S.P., *et al.*: 2008, *Space Sci. Rev.* **136**, 67.

Hurlburt, N., Cheung, M., Schrijver, C., Chang, L., Freeland, S., Green, S., Heck, C., Jaffey, A., Kobashi, A., Schiff, D., Serafin, J., Seguin, R., Slater, G., Somani, A., Timmons, R.: 2012, *Solar Phys.* **275**, 67. ADS:2012SoPh..275...67H. doi:10.1007/s11207-010-9624-2.

Isobe, T., Feigelson, E.D., Akritas, M.G., Babu, G.J.: 1990, *Astrophys. J.* **364**, 104.

Martens, P.C.H., Attrill, G.D.R., Davey, A.R., Engell, A., Farid, S., Grigis, P.C., Kasper, J., Korreck, K., *et al.*: 2012, *Solar Phys.* **275**, 79. ADS:2012SoPh..275...79M. doi:10.1007/s11207-010-9697-y.

Mewaldt, R.A., Cohen, C.M.S., Mason, G.M., von Rosenvinge, T.T., Leske, R.A., Luhmann, J.G., Odstrcil, D., Vourlidas, A.: 2013, In: Zank, G.P., Borovsky, J., Bruno, R., Cirtain, J., Cranmer, S., Elliott, H., Giacalone, J., Gonzalez, W., Li, G., Marsch, E., Moebius, E., Pogorelov, N., Spann, J., Verkhoglyadova, O. (eds.) *Solar Wind 13* **CP-1539**, 116. doi:10.1063/1.4811002.

Nitta, N.V., Aschwanden, M.J., Boerner, P.F., Freeland, S.L., Lemen, J.R., Wülser, J.P.: 2013, *Solar Phys.* doi:10.1007/s11207-013-0307-7.

Rouillard, A.P., Sheeley, N. R Jr., Tylka, A., Vourlidas, A., Ng, C.K., Rakowski, C., Cohen, C.M.S., Mewaldt, R.A., *et al.*: 2012, *Astrophys. J.* **752**, 44.

Thompson, W.T. 2006, *Astron. Astrophys.* **449**, 791.

Thompson, W.T.: 2010, *Astron. Astrophys.* **515**, A59.

Thompson, W.T., Wei, K.: 2010, *Solar Phys.* **261**, 215.

Veronig, A.M., Muhr, N., Kienreich, I.W., Temmer, M., Vrsnak, B.: 2010, *Astrophys. J. Lett.* **716**, L57.

Watanabe, K., Masuda, S., Segawa, T.: 2012, *Solar Phys.* **279**, 317. ADS:2012SoPh..279..317W. doi:10.1007/s11207-012-9983-y.

Wülser, J.P., Lemen, J.R., Tarbell, T.D., Wolfson, C.J., Cannon, J.C., Carpenter, B., *et al.*: 2004, *Proc. SPIE* **5171**, 111.